

Highly Exposed Active Sites of Defect-Enriched Derived MOFs for Enhanced Oxygen Reduction Reaction

Yu Zhu,^{†,‡} Zeyi Zhang,^{†,‡} Wenqiang Li,[§] Zhao Lei,^{†,‡} Niancai Cheng,^{*,†,‡,§} Yangyang Tan,^{†,‡} Shichun Mu,^{||} and Xueliang Sun^{*,†,‡,||}

[†]College of Materials Science and Engineering and [‡]Key Laboratory of Eco-materials Advanced Technology, Fuzhou University, No. 2 Xueyuan Street, Fuzhou 350108, China

[§]Henan Key Laboratory of Function-Oriented Porous Materials, College of Chemistry and Chemical Engineering, Luoyang Normal University, Luoyang 471934, China

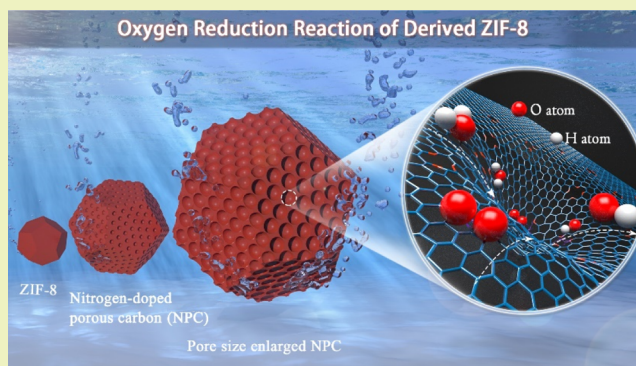
^{||}State Key Laboratory of Advanced Technology for Materials Synthesis and Processing, Wuhan University of Technology, Wuhan 430070, China

[‡]Department of Mechanical and Materials Engineering, The University of Western Ontario, London, Ontario N6A 5B9, Canada

Supporting Information

ABSTRACT: The low utilization of active sites of metal–organic framework (MOF)-derived nanostructured carbon materials are considerable challenges in practical applications. Here, we develop MOF (ZIF-8)-derived N-doped porous carbon (NPC) nanomaterials as high active oxygen reduction reaction (ORR) catalysts which are enhancing both the exposed active sites and surface defects of NPC resulting from the enlarged pore of NPC by KOH activation strategy. The experiments show that the KOH activation not only enlarged the pore size of ZIF-8-derived NPC nanomaterials creating numerous mesopores but also generated abundant defects in NPC nanomaterials. The 4 h KOH-activated MOF-derived NPC (NPC-4) nanomaterials show an activity of 0.257 mA cm⁻² at 0.9 V (vs reversible hydrogen electrode), which was almost 10 times greater than that of NPC nanomaterials (0.0265 mA cm⁻²). The NPC-4 exhibits a comparable ORR activity, higher stability, and better tolerance to methanol compared with the commercial Pt/C. The density functional theory results show that N-doped carbon along with the defects is more favorable for ORR compared with N-doped carbon because the presence of defects leads to enhanced O adsorption ability and promotes the ORR process.

KEYWORDS: N-doped porous carbon, active sites, defect, oxygen reduction reaction, fuel cells



INTRODUCTION

Metal–organic framework (MOF)-derived carbon nanomaterials have attracted considerable attention in catalysis owing to their superior properties, such as high surface area, large pore volumes, excellent chemical stabilities, and an excellent electrical conductivity.^{1–6} Especially, MOF-derived N-doped porous carbon (NPC) nanomaterials have been widely investigated as oxygen reduction reaction (ORR) electrocatalysts to avoid or minimize the use of precious metals such as Pt in fuel cells.^{7–11} N-doped carbon (N–C) or N-coordinated metals on NPC nanomaterials can be achieved as a highly ORR active sites by pyrolysis of various MOFs precursors.^{12–15} The surface area and porosity of MOF-derived NPC nanomaterials plays an important role in determining their ORR catalytic properties. The best ORR performance of catalysts derived from MOF precursors were usually obtained through optimizing the porosity and surface area of those derived catalysts.^{16–18}

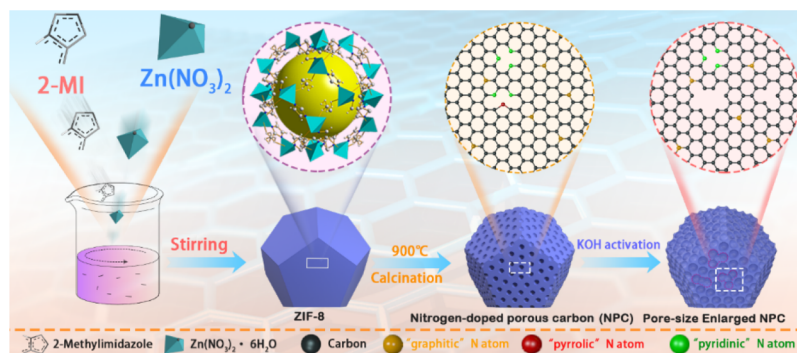
Although MOF-derived NPC nanomaterials possess high porosity and large surface area with numerous active sites, how to create highly exposed active sites and thus improve the utilization of active sites of MOF-derived NPCs still remains a big challenge. Generally, a high surface area with the maximum exposed active sites to the electrolyte is crucial for the performance of nanoporous electrode materials.¹⁹ Numerous N-containing active sites can be easily obtained by the direct pyrolysis/carbonization of MOFs with N-containing ligands at high temperatures. N-containing active sites are uniformly distributed throughout of MOF-derived NPC nanomaterials with a significant thickness, and most of those N-containing active sites are mainly located at the micropore surface inside MOF-derived NPC nanomaterials.^{20,21} The utilization of active

Received: July 29, 2019

Revised: August 17, 2019

Published: August 29, 2019

Scheme 1. Schematic Diagram of the Synthesis of the Pore Size-Enlarged NPC Nanomaterials Derived from ZIF-8 Precursors



sites inside MOF-derived NPC catalysts are hindered by the limited mass transfer because of small pore size, disorder, and their lengthy diffusion path.^{18,22} There are large transfer resistance for reactants (such as oxygen) to reach the active sites inside MOF-derived NPC nanomaterials through micropores which decrease the utilization of active sites of MOF-derived nanomaterials.^{23,24} The optimizing porosity of MOF-derived NPC nanomaterials creating mesopores by NH_3 activation showed higher ORR performance compared with nanomaterials derived from their pure MOFs due to a faster mass transfer,^{25,26} Xie et al. reported a biomass-derived hierarchical porous carbon material by KOH activation with unique porous structural properties as electrode materials.²⁷ Recently, experiments and theoretical calculations demonstrated that adjusting surface defects in the carbon nanomaterials is one of most effective strategies to enhance the ORR activity.^{28–31} Therefore, it is desirable to explore an effective way to enlarge the pore size of MOF-derived NPC nanomaterials generating mesopores and defects and thus providing more exposed active sites and facilitating the mass transfer to enhance the ORR activity.

Here, we demonstrate a novel strategy to enhance the ORR activity of MOF-derived nanomaterials through enlarging the pore size and adjusting surface defects of the MOF-derived NPC nanomaterials by the KOH activation. In this work, the Zn-based zeolitic imidazolate framework (ZIF-8) is used as a mode MOFs to produce NPC nanomaterials. The experiments show that the KOH activation not only enlarged the pore size of ZIF-8-derived NPC nanomaterials but also generated defects in NPC nanomaterials, which expose more active sites and facilitate the mass transfer of ORR reactants. The pore-enlarged ZIF-8-derived NPC nanomaterials have higher ORR activity than the pure ZIF-8-derived NPC.

EXPERIMENTAL SECTION

Synthesis of Pore Size-Enlarged NPC Derived from the ZIF-8 Precursor. The ZIF-8 was synthesized according to a reported procedure.³² The as-prepared ZIF-8 was grounded into a powder and transferred into a quartz tube, followed by the heat treatment temperature 900 °C for 2 h under a N_2 atmosphere, and the obtained black powder is washed with 1 M HCl and then washed with deionized water three times (labeled as NPC). For the KOH activation process, a mass ratio of 1:1 of NPC and KOH was added in 15 mL of deionized water and ultrasonicated for 1 h. Then, the suspension was evaporated to form a smooth and thick slurry by heating under magnetic stirring at 80 °C, followed by drying at 60 °C in a vacuum oven. After being ground in an agate mortar, samples were heated in a tube furnace at 750 °C for 1, 2, 4, and 5 h (labeled as NPC-1, NPC-2, NPC-4, and NPC-5, respectively) at a N_2 atmosphere. The resulting products were first washed with 1 M

HCl and then washed with deionized water three times, followed by drying 70 °C in a vacuum oven.

Materials Characterization. The morphology and structure of the samples were characterized by scanning electron microscopy (SEM, Supra 55), transmission electron microscopy (TEM, Tecnai G2F20), and X-ray powder diffraction (Ultima III). X-ray photoelectron spectroscopy (XPS) characterization was performed by a K-Alpha. Nitrogen adsorption–desorption isotherms were determined by the Brunauer–Emmett–Teller (BET) equation using the equipment of Micromeritics 3Flex. Material surface analysis was determined by Raman.

Electrochemical Testing. All electrochemical measurements were carried out at room temperature using an Autolab electrochemistry station in a standard three-electrode cell. A catalyst modified glassy carbon electrode was used as the working electrode. Ag/AgCl (sat. KCl) and platinum wire were used as the reference and counter electrodes, respectively. The working electrodes were prepared as follows: The catalyst slurry was prepared by mixing 5.0 mg of catalyst in 350 μL of ethanol and 150 μL of water and 50 μL of Nafion (5 wt %) and then ultrasonicated for 15 min to form a uniform black ink. Subsequently, 5.6 μL of prepared catalyst ink was pipetted onto a rotating disk electrode (RDE, 3.00 mm diameter). For the commercial Pt/C (20 wt %), 3.0 mg of sample was added in 3 mL of deionized water that contained 10 μL of Nafion (5 wt %), followed by ultrasonication for 15 min, and then, 3.6 μL of ink was pipetted onto RDE. The potentials presented in this study are referred with respect to the reversible hydrogen electrode (RHE). Cyclic voltammetry measurements were performed at a scan rate of 10 $\text{mV}\cdot\text{s}^{-1}$ within a potential range from 0.05 to 1.2 V (vs RHE) in 0.1 M KOH. ORR linear sweep voltammetry (LSV) measurements were conducted on a RDE in O_2 -saturated 0.1 M KOH solution at a scan rate of 10 $\text{mV}\cdot\text{s}^{-1}$ and at rotating speed of 1600 rpm. The electrochemical impedance spectroscopy (EIS) are recorded in O_2 -saturated 0.1 M KOH at 0.82 V (vs RHE) with 5 mV ac potential from 10 kHz to 0.01 Hz (rotation speed: 1600 rpm). Methanol tolerability tests were performed in 0.1 M KOH-contained 1 M methanol. Accelerated durability tests (ADT) were performed by sweeping the electrode between 0.6 and 1.0 V (vs RHE) at 50 $\text{mV}\cdot\text{s}^{-1}$ for 10 000 cycles in oxygen saturated 0.1 M KOH.

Density Functional Theory Calculation. Geometric optimization and total energy calculations were performed within the density functional theory (DFT) framework as implemented with a Vienna ab initio simulation package (VASP) in which spin-polarization was all considered.^{33–36} We used the projector-augmented wave potentials' database to simulate the interaction between valence electrons and cores.^{37,38} In addition, the Perdew–Burke–Ernzerhof of exchange correlational function and the generalized-gradient approximation was adopted to investigate the transfer and correlation of electrons.³⁹ It is reasonable to choose the kinetic energy cutoff for plane wave expansion at 450 eV and a $2 \times 2 \times 1$ Monkhorst–Pack k -point grid sampling of the first Brillouin zone.⁴⁰ In order to determine the occupancy, we set the Gaussian smearing width to 0.1 eV. The adsorption surface, of which the unit lattice constant is set to 12.792 Å \times 14.772 Å and the vacuum layer is set to 15 Å, was calculated the structural relaxation by using a conjugate gradient algorithm, limiting

the maximum force and energy of unconstrained atoms to less than 0.01 eV/Å and 1×10^{-5} eV, respectively. The electronic iteration convergence value for self-consistent field calculation was set to 1×10^{-4} eV.

RESULTS AND DISCUSSION

The fabrication strategy of the pore size-enlarged NPC nanoparticles derived from ZIF-8 precursors is schematically illustrated in Scheme 1. First, the average particle size of prepared ZIF-8 is 40–50 nm (Figure S1). The ZIF-8 crystals are converted into N-doped graphitic porous carbon nanomaterials retaining its original morphology after carbonization at 900 °C under a N₂ atmosphere (Figure S2). After KOH activation, it is obvious that a much rougher surface formed on the KOH-activated NPC nanoparticles in comparison with parent ZIF-8-derived NPC. The surface roughness of NPC nanoparticles increases with the time of KOH activation (Figures 1 and S3–S5), mainly originating from the generation of numerous surface defects on the NPC.⁴¹

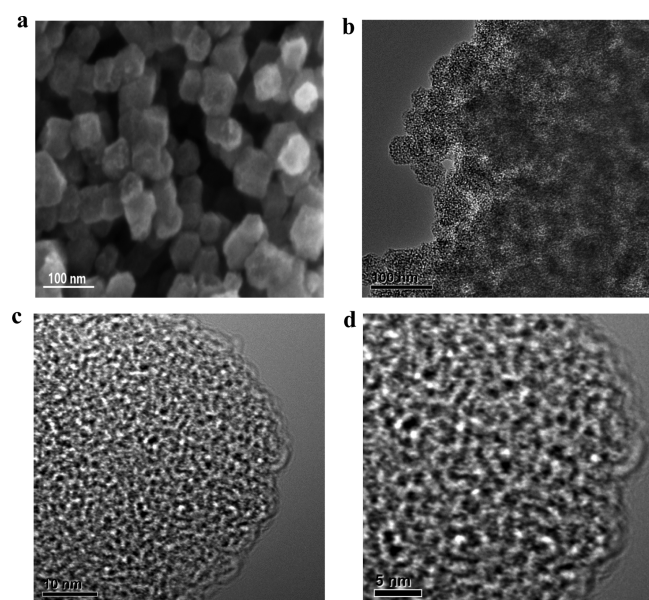


Figure 1. (a) SEM image of NPC-4 sample, (b) low-resolution and (c,d) high-resolution TEM images of the NPC-4 sample.

More importantly, we found that the pore size of ZIF-8-derived NPC nanoparticles enlarged after KOH activation and the pore size increases with prolonged time of KOH activation. As shown in Figure S3, it is observed that most pores formed on the surface of ZIF-8-derived NPC nanoparticles are micropores (in red cycle). Some larger pores (>1 nm) were found on the surface for 1 and 2 h KOH-activated ZIF-8-derived NPC nanoparticles (Figures S3 and S4). When the activation time is prolonged to 4 h, micropores decrease and most of the pore size is more than 1 nm on the surface of NPC-4 nanoparticles (Figure 1c,d). Furthermore, mesopores formed in NPC-4 nanoparticles. It is worth to mention that larger pores in KOH-activated ZIF-8-derived NPC formed through coalescing of unconnected micropores of NPC. These findings suggest that KOH activation is a good strategy to enlarge the pore size of MOF-derived NPC nanomaterials.⁴² However, it is very important to control the KOH activation time, and the framework of ZIF-8-derived NPC nanoparticles collapsed during the KOH activation process when KOH

activation time increases to 5 h (Figure S5). The framework collapse of NPC-5 will lower the mass transfer and thus decrease the ORR activity.^{43,44}

The pore structure of nanoporous electrode materials plays an important role in determining the ORR activity because the pore size will affect diffusion of reactants and mass transport.^{45,46} The nitrogen adsorption–desorption isotherms were used to further investigate the details of pore size change of KOH-activated ZIF-8-derived NPC nanoparticles. The isotherms as shown in Figure 2a indicate that the 4 h KOH activation can obviously increase the BET surface area of ZIF-8-derived NPC nanoparticles. More importantly, compared with the NPC sample, the distinct hysteresis loop in the range of P/P_0 0.4–0.8 for the NPC-4 sample suggests that 4 h KOH activation significantly increases the mesopore (pore size of 2–50 nm) of the NPC sample,^{47,48} which is beneficial for mass transfer through the entire NPC and promotes the interfacial catalytic reaction. The pore size distribution (PSD) plots indicated that the pore size obviously increased for the KOH activated NPC nanomaterials (Figure 2b), which is in accord with the result of TEM images. The NPC-4 nanomaterials possessed ultramicropore, micropore and mesopore centered at 0.7, 1.2, and 2.8 nm, respectively, while the ZIF-8-derived NPC nanomaterials mainly have micropore structure with pore size between 0.5 and 1 nm (Figure 2b). It is well known that MOF-derived nanomaterials with abundant mesopores can provide a favorable mass transport platform and expose more active sites.⁴ To understand how the mesopore formed in NPC-4 nanomaterials, we carefully check the pore size of different KOH time activated NPCs. After 1 h KOH activation, the micropore centered at 1.2 nm increased and mesopore centered at 2.3 nm formed on the NPC-1 samples (Figure S6). In addition, some pore size (<0.5 nm) appeared. When the KOH activation time increases to 2 h, the pore size ranging from 1 to 4 nm increased compared with the NPC-1 samples (Figure S6). It is obvious that the pore size (<1 nm) decreased when KOH activation time increases to 5 h (Figure S6). The surface area and pore area characteristics of NPC and KOH-activated NPC samples are summarized in Table 1. The KOH activation can first create micropores on the surface of NPC through the etching reaction between KOH and carbon, confirmed by the analysis of BET results. The size of newly generated micropores increase with the etching reaction and then enlarge or coalesce the unconnected micropores of NPC to new mesopores with the increase in the activation time (Scheme 1). The mechanism of KOH activation for the enlarged pore structure of NPC materials may be considered as the etching reaction of carbon in ZIF-8-derived NPC according to the following eq 1⁴⁹



The nanoporous electrode materials containing both micropores and mesopores will increase the utilization of active sites because mesopores facilitate the mass transfer, whereas micropores provide numerous accessible active sites.⁵⁰ BET results further confirm that the KOH activation is an effective way to enlarge the pore size of MOF-derived NPC nanomaterials to create numerous mesopores and expose more active sites, thus increasing the utilization of active sites within whole nonporous catalysts.

XPS measurements were used to analyze the surface chemical states of KOH-activated ZIF-8-derived NPC nanomaterials. Figure S7 shows the XPS survey spectra of KOH-

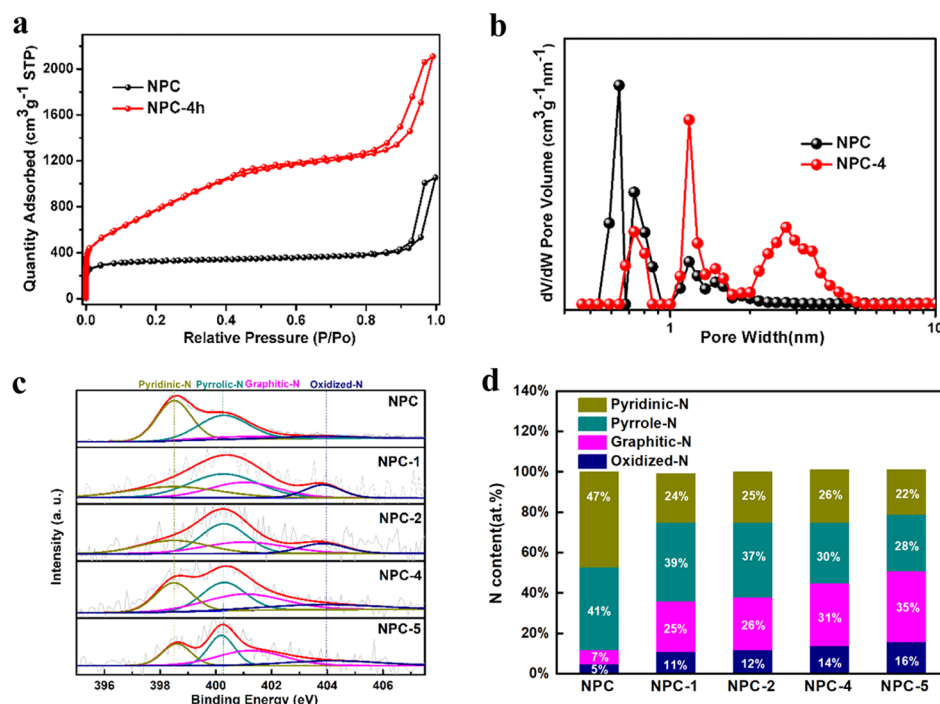


Figure 2. (a) N₂ adsorption–desorption isotherms of ZIF-8-derived NPC nanomaterial and KOH-activated ZIF-8-derived NPC nanomaterials. (b) PSD data obtained by the DFT method of NPC and NPC-4 samples. (c) High-resolution N 1s spectra and (d) the contents of four kinds of nitrogen species of ZIF-8-derived NPC nanomaterial and KOH-activated ZIF-8-derived NPC nanomaterials.

Table 1. Surface Area and Pore Area Characteristics of NPC, NPC-1, NPC-2, NPC-4, and NPC-5

sample	surface area (m ² g ⁻¹)	micropore area (m ² g ⁻¹)	mesopore area (m ² g ⁻¹)	S _{Meso} /S _{BET} (%)
NPC	1003	936	67	6.7
NPC-1	3077	2461	616	20
NPC-2	3074	2360	714	23.2
NPC-4	2928	2047	881	30
NPC-5	2818	1862	956	33.9

activated ZIF-8-derived NPC nanomaterials. The high-resolution N 1s spectra of NPC nanomaterials as shown in Figure 2c displays the existence of four nitrogen species: pyridinic-N (~398.6 eV), pyrrolic-N (~400.1 eV), graphitic-N (~401.2 eV), and oxidized-N (~404.1 eV). It is believed that pyridinic-N or graphitic-N species are the dominant active sites for ORR.^{51–56} We found that the content of different N types of as-prepared samples change with the KOH activation

(Figure 2d). After 1 h KOH activation, the contents of pyridinic-N and pyrrolic-N decrease while the contents of graphitic-N and oxidized-N slight increase, which may be attributed to the different KOH etching speeds for various N–C configurations. With prolonged time KOH activation, the NPC-2 samples have 25% pyridinic-N and 26% graphitic-N, whereas the NPC-4 samples possess 26% pyridinic-N and 31% graphitic-N. Therefore, the NPC-4 nanomaterials contain more pyridinic-N and graphitic-N atoms than other KOH-activated NPC samples, which are considered to be highly active sites for the ORR.¹² Figure 3a displays the Raman spectra of KOH-activated ZIF-8-derived NPC nanomaterials with a typical D-band (~1350 cm⁻¹) and G-band (~1580 cm⁻¹) corresponding to the disordered carbon and the highly ordered graphitic carbon, respectively.^{57,58} The intensity ratio (I_D/I_G) of NPC is 0.95, and the ratio of I_D/I_G gradually increases to 1.08 with the KOH etching time, indicating that the KOH activation generates the defects in NPC. The more defects in KOH-activated NPC are further confirmed by the X-

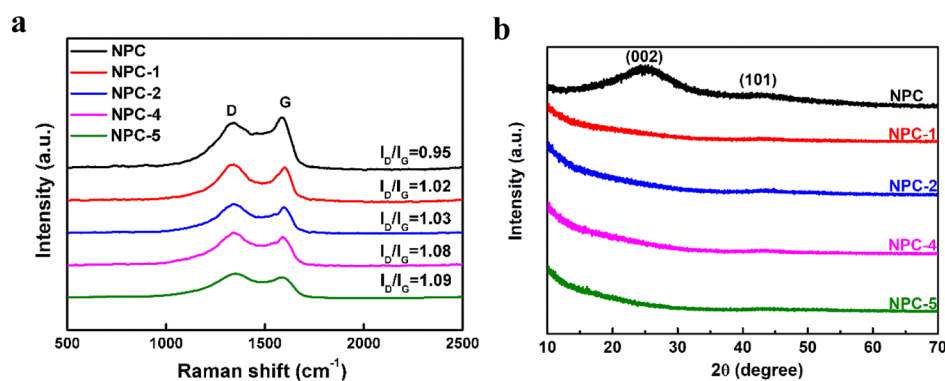


Figure 3. (a) Raman spectra and (b) XRD of the ZIF-8-derived NPC nanomaterial and KOH-activated ZIF-8-derived NPC nanomaterials.

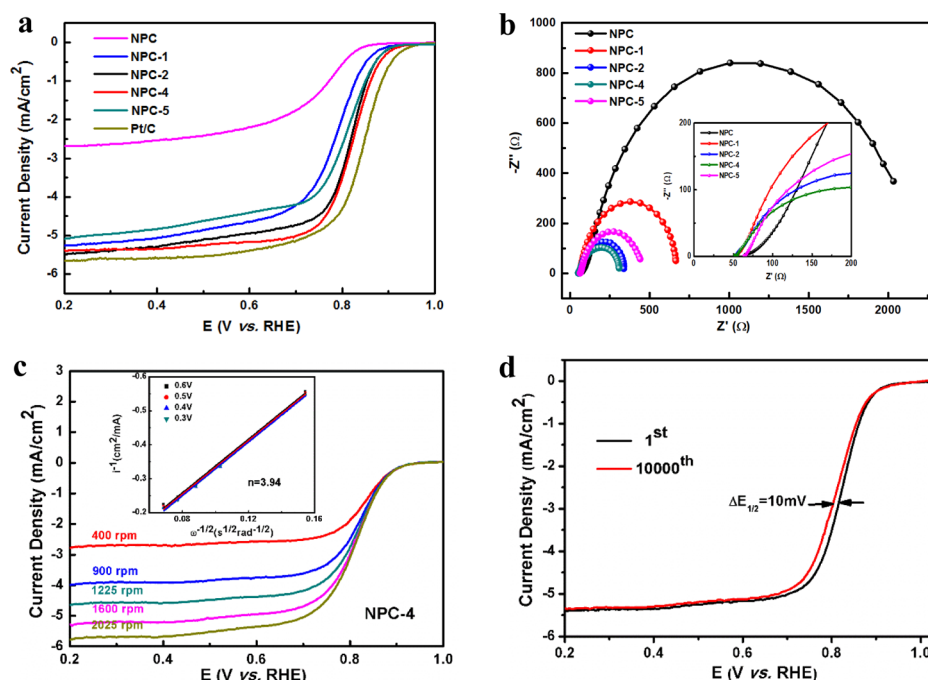


Figure 4. (a) Linear sweep voltammograms of ZIF-8-derived NPC nanomaterial, KOH-activated ZIF-8-derived NPC nanomaterials and Pt/C (20%) in O₂-saturated 0.1 M KOH solution at a scan rate of 10 mV·s⁻¹ with 1600 rpm. (b) EIS of ZIF-8-derived NPC nanomaterial and KOH-activated ZIF-8-derived NPC nanomaterials. (c) LSV curves of NPC-4 in O₂-saturated 0.1 M KOH with various rotation speeds at a scan rate of 10 mV·s⁻¹, with the inset giving the K–L plots. (d) ORR curves of electrodes made from NPC-4 in O₂-saturated 0.1 M KOH at a scan rate of 10 mV·s⁻¹ with 1600 rpm during the durability tests.

ray diffraction (XRD) patterns (Figure 3b). NPC displayed two broad peaks at 25° and 43°, corresponding to the (002) and (101) planes of graphitic carbon, whereas KOH-activated NPC shows very weak peaks at 25° and 43°, suggesting that the KOH activation can generate defects on the surface of NPC. Our finding is also in consistent with the previous studies, which shows that the KOH activation can effectively generate the defects on carbon materials.⁴¹ It is observed that abundant defects on the carbon material can serve as efficient active sites for ORR.^{53,59,60}

The electrochemical performance of the as-prepared samples was carried out to investigate the effects of the KOH activation on NPC nanomaterials as electrochemical catalysts toward ORR. The NPC nanomaterials without KOH activation show poor ORR activity with a large overpotential (Figure 4a). The KOH activation can gradually enhance the ORR activity with an increased activation time ranging from 1 to 4 h (Figure 4a). The ORR activity of NPC-4 nanomaterials at 0.9 V is 0.257 mA cm⁻², which was almost 10 times greater than that of NPC nanomaterials (0.0265 mA cm⁻²). The NPC-4 nanomaterials exhibited highest catalytic activities toward ORR, which is comparable to that of Pt/C catalysts. In addition, the Tafel slopes for NPC-4 and Pt/C were observed to be very similar (Figure S8). However, it was observed that the ORR catalytic activity of the NPC-5 nanomaterials decreased (Figure 4a). This is likely ascribed to the collapse of the ZIF-8-derived NPC framework consistent with the analysis of TEM images, which will decrease the ORR activity because of the increase in the mass transport resistance. Therefore, it is very important to control the KOH activation time to keep NPC morphology and optimize porosity. The enhanced ORR activity of NPC-4 nanomaterials should be attributed to the more active sites resulting from optimization of N species and enlarged pore of

NPC, which create numerous mesopores, facilitating the mass transfer of ORR reactants and increasing the utilization of active sites. The EIS measurements (Figure 4b) also reveal that the NPC-4 has much lower charge-transfer resistance and intrinsic resistance compared with the other as-prepared samples. To further investigate the ORR kinetics of the NPC-4 samples, LSV polarization curves at various rotating rates are performed using a RDE. The *n* value for the NPC-4 sample is calculated to be 3.94 according to the slope of K–L plots in the potential range of 0.3–0.6 V (Figure 4c), which is close to the four-electron ORR process. Comparison of ORR activities of the NPC-4 catalyst and latest N-doped carbon catalysts reported previously further verifies that our synthesis strategy is very effective in improving the ORR performance (Table S1).

The evaluation of stability is crucial for the development of new electrocatalysts for practical application. The ADTs were conducted using a thin-film catalyst coated on a RDE. The electrode potential was cycled between 0.6 and 1.0 V (vs RHE) at 50 mV·s⁻¹ for 10 000 cycles in oxygen saturated 0.1 M KOH. It is observed that the NPC-4 catalyst is more stable than the commercial Pt/C catalyst. After 10 000 cycles, the *E*_{1/2} value of the NPC-4 catalyst exhibits a small negative shift of 10 mV (Figure 4d), whereas the commercial Pt/C catalyst shows a larger negative shift of 41 mV during potential cycling (Figure S9). Furthermore, compared with Pt/C catalyst, the NPC-4 catalyst shows better tolerance to the methanol poison (Figure S10), suggesting an excellent ORR selectivity.

To further explore the intrinsic ORR catalytic mechanism of the N-doped carbon, DFT calculations are carried out to determine the dominant catalytic sites of different doping configurations. We first used principles DFT calculations to evaluate graphitic-N and pyridinic-N species toward ORR

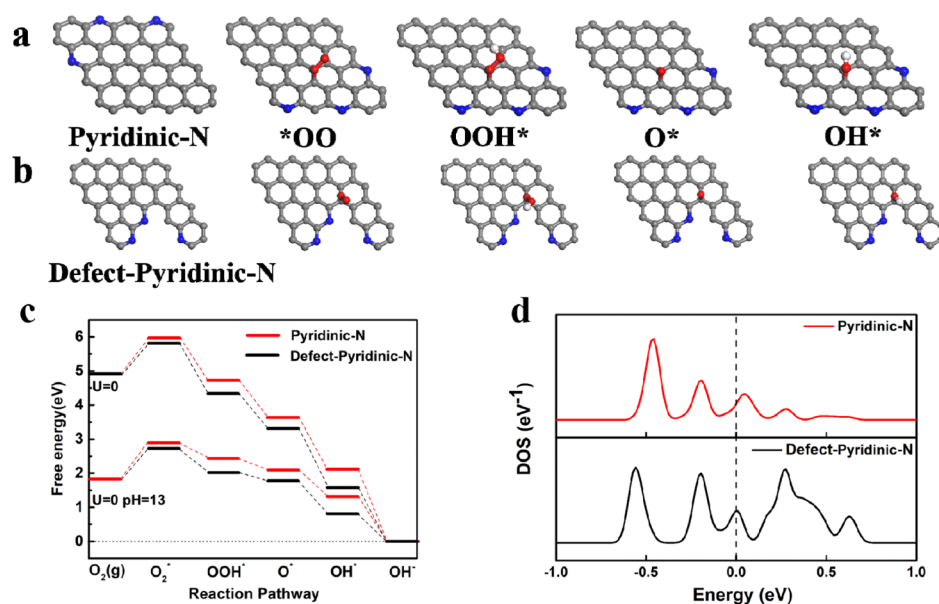


Figure 5. (a) Pyridinic-N and (b) pyridinic-N in defect models in the ORR different step process. (c) Free-energy of different N structures. (d) Density of states of pyridinic-N in the defect models and pyridinic-N models.

activity in alkaline solution. The calculated free-energy profiles on these two N doping configurations are shown in Figure S11. Our DFT study predicted that the ORR catalytic activity of the graphitic-N species is similar to the pyridinic-N species in alkaline media. To study the influence of N-doped carbon nanomaterials along with the defects, we calculated the ORR processes on pyridinic-N and defect-pyridinic-N models (Figure 5a,b). In alkaline media, after the O_2 molecule first adsorbed on the top of the active sites on the NPC-4 sample, O_2 will be protonated to form OOH* , the OOH* will then dissociate into O* and OH* , and finally both O* and OH* form product OH^- .⁶¹ The oxygen molecules adsorbed on the surface of catalysts as the initial step play an important role in the ORR activity.⁵¹ Figure 5c reveals that the defect-pyridinic-N has lower energy barrier for O_2 chemisorption in first step of the ORR process ($\text{O}_2 + * \rightarrow \text{O}_2^*$), which will benefit for the high ORR activity. Moreover, the rate-determining step for the ORR process ($\text{OH*} + \text{e}^- \rightarrow \text{OH}^-$) has a lower overpotential in defect-pyridinic-N. Those data suggested that the defects on KOH-activated NPC will facilitate the ORR process. As shown in Figure 5d, the increased electronic states around the Fermi level in defect-pyridinic-N may be ascribed to the formation of defects around pyridinic-N, leading to the enhanced O adsorption ability and thereby the ORR activity. In summary, the presence of the defect structure helps to improve the ORR activity in alkaline electrolytes.

CONCLUSION

In conclusion, we successfully synthesized a highly active ORR metal-free N-doped carbon catalyst through both enlarging the pore size and generating surface defects of the ZIF-8-derived NPC nanomaterials by KOH activation. The 4 h KOH-activated MOF-derived NPC (NPC-4) nanomaterials show an activity almost 10 times higher than that of NPC nanomaterials. It is found that the optimized NPC-4 exhibits comparable ORR catalytic activity, higher stability, and better tolerance to methanol compared with the commercial Pt/C. The enhanced ORR activity of NPC-4 nanomaterials is attributed to the abundant surface defects and the highly exposed active sites

enabled by KOH activation creating numerous mesopores, which facilitate the mass transfer of ORR reactants. The DFT results show that N-doped carbon along with the defects is more favorable for ORR compared with N-doped carbon because the presence of a defect leads to enhanced O adsorption ability and promotes the ORR process. We believe that the general synthetic strategy presented here can be extended to other catalytic systems, increasing the exposed of active sites.

ASSOCIATED CONTENT

Supporting Information

The Supporting Information is available free of charge on the ACS Publications website at DOI: 10.1021/acssuschemeng.9b04380.

SEM images, XRD patterns, TEM images, nitrogen adsorption–desorption isotherms, XPS spectra, Tafel plots, durability tests, methanol poison tests, free-energy profiles, and comparison of ORR activities (PDF)

AUTHOR INFORMATION

Corresponding Authors

*E-mail: niancaicheng@fzu.edu.cn (N.C.).

*E-mail: xsun@eng.uwo.ca (X.S.).

ORCID

Niancai Cheng: 0000-0002-6358-5515

Shichun Mu: 0000-0003-3902-0976

Xueliang Sun: 0000-0003-2881-8237

Notes

The authors declare no competing financial interest.

ACKNOWLEDGMENTS

This work was supported by the National Natural Science Foundation of China (grant no. 21875039), Minjiang Professorship (XRC-1677), Fujian province's high level innovative and entrepreneurial talents (50012709), and the Open Project Program of the State Key Laboratory of

Photocatalysis on Energy and Environment (grant no. SKLPEE-201814), Fuzhou University.

REFERENCES

- (1) Liu, J.; Zhu, D.; Guo, C.; Vasileff, A.; Qiao, S.-Z. Design Strategies toward Advanced MOF-Derived Electrocatalysts for Electrochemical Reactions. *Adv. Eng. Mater.* **2017**, *7*, 1700518–1700544.
- (2) Jiang, M.; Cao, X.; Zhu, D.; Duan, Y.; Zhang, J. Hierarchically Porous N-doped Carbon Derived from ZIF-8 Nanocomposites for Electrochemical Applications. *Electrochim. Acta* **2016**, *196*, 699–707.
- (3) Zhao, Y.; Song, Z.; Li, X.; Sun, Q.; Cheng, N.; Lawes, S.; Sun, X. Metal organic frameworks for energy storage and conversion. *Energy Storage Mater.* **2016**, *2*, 35–62.
- (4) Huang, X.; Zhang, Y.; Shen, H.; Li, W.; Shen, T.; Ali, Z.; Tang, T.; Guo, S.; Sun, Q.; Hou, Y. N-Doped Carbon Nanosheet Networks with Favorable Active Sites Triggered by Metal Nanoparticles as Bifunctional Oxygen Electrocatalysts. *ACS Energy Lett.* **2018**, *3*, 2914–2920.
- (5) Wang, Y.; Pan, Y.; Zhu, L.; Yu, H.; Duan, B.; Wang, R.; Zhang, Z.; Qiu, S. Solvent-free assembly of Co/Fe-containing MOFs derived N-doped mesoporous carbon nanosheet for ORR and HER. *Carbon* **2019**, *146*, 671–679.
- (6) Xuan, C.; Peng, Z.; Xia, K.; Wang, J.; Xiao, W.; Lei, W.; Gong, M.; Huang, T.; Wang, D. Self-supported ternary Ni-Fe-P nanosheets derived from metal-organic frameworks as efficient overall water splitting electrocatalysts. *Electrochim. Acta* **2017**, *258*, 423–432.
- (7) Zhang, H.; Osgood, H.; Xie, X.; Shao, Y.; Wu, G. Engineering nanostructures of PGM-free oxygen-reduction catalysts using metal-organic frameworks. *Nano Energy* **2017**, *31*, 331–350.
- (8) Chen, Y.-Z.; Wang, C.; Wu, Z.-Y.; Xiong, Y.; Xu, Q.; Yu, S.-H.; Jiang, H.-L. From Bimetallic Metal-Organic Framework to Porous Carbon: High Surface Area and Multicomponent Active Dopants for Excellent Electrocatalysis. *Adv. Mater.* **2015**, *27*, 5010–5016.
- (9) Ning, H.; Li, G.; Chen, Y.; Zhang, K.; Gong, Z.; Nie, R.; Hu, W.; Xia, Q. Porous N-Doped Carbon-Encapsulated CoNi Alloy Nanoparticles Derived from MOFs as Efficient Bifunctional Oxygen Electrocatalysts. *ACS Appl. Mater. Interfaces* **2019**, *11*, 1957–1968.
- (10) Yang, L.; Feng, S.; Xu, G.; Wei, B.; Zhang, L. Electrospun MOF-Based FeCo Nanoparticles Embedded in Nitrogen-Doped Mesoporous Carbon Nanofibers as an Efficient Bifunctional Catalyst for Oxygen Reduction and Oxygen Evolution Reactions in Zinc-Air Batteries. *ACS Sustainable Chem. Eng.* **2019**, *7*, 5462–5475.
- (11) Ye, G.; Zhao, K.; He, Z.; Huang, R.; Liu, Y.; Liu, S. Fe-Nx Sites Enriched Carbon Micropolyhedrons Derived from Fe-Doped Zeolitic Imidazolate Frameworks with Reinforced Fe-N Coordination for Efficient Oxygen Reduction Reaction. *ACS Sustainable Chem. Eng.* **2018**, *6*, 15624–15633.
- (12) Barkholtz, H. M.; Liu, D.-J. Advancements in rationally designed PGM-free fuel cell catalysts derived from metal-organic frameworks. *Mater. Horiz.* **2017**, *4*, 20–37.
- (13) Shen, K.; Chen, X.; Chen, J.; Li, Y. Development of MOF-Derived Carbon-Based Nanomaterials for Efficient Catalysis. *ACS Catal.* **2016**, *6*, 5887–5903.
- (14) Song, Z.; Cheng, N.; Lushington, A.; Sun, X. Recent Progress on MOF-Derived Nanomaterials as Advanced Electrocatalysts in Fuel Cells. *Catalysts* **2016**, *6*, 116–135.
- (15) Li, R.; Wang, X.; Dong, Y.; Pan, X.; Liu, X.; Zhao, Z.; Qiu, J. Nitrogen-doped carbon nanotubes decorated with cobalt nanoparticles derived from zeolitic imidazolate framework-67 for highly efficient oxygen reduction reaction electrocatalysis. *Carbon* **2018**, *132*, 580–588.
- (16) Wang, X.; Zhou, J.; Fu, H.; Li, W.; Fan, X.; Xin, G.; Zheng, J.; Li, X. MOF derived catalysts for electrochemical oxygen reduction. *J. Mater. Chem. A* **2014**, *2*, 14064–14070.
- (17) Zhang, L.; Su, Z.; Jiang, F.; Yang, L.; Qian, J.; Zhou, Y.; Li, W.; Hong, M. Highly graphitized nitrogen-doped porous carbon nanopolyhedra derived from ZIF-8 nanocrystals as efficient electrocatalysts for oxygen reduction reactions. *Nanoscale* **2014**, *6*, 6590–6602.
- (18) You, S.; Gong, X.; Wang, W.; Qi, D.; Wang, X.; Chen, X.; Ren, N. Enhanced Cathodic Oxygen Reduction and Power Production of Microbial Fuel Cell Based on Noble-Metal-Free Electrocatalyst Derived from Metal-Organic Frameworks. *Adv. Eng. Mater.* **2016**, *6*, 1501497–1501506.
- (19) Xia, W.; Mahmood, A.; Zou, R.; Xu, Q. Metal-organic frameworks and their derived nanostructures for electrochemical energy storage and conversion. *Energy Environ. Sci.* **2015**, *8*, 1837–1866.
- (20) Proietti, E.; Jaouen, F.; Lefèvre, M.; Larouche, N.; Tian, J.; Herranz, J.; Dodelet, J.-P. Iron-based cathode catalyst with enhanced power density in polymer electrolyte membrane fuel cells. *Nat. Commun.* **2011**, *2*, 416–425.
- (21) Ye, Y.; Cai, F.; Li, H.; Wu, H.; Wang, G.; Li, Y.; Miao, S.; Xie, S.; Si, R.; Wang, J.; Bao, X. Surface functionalization of ZIF-8 with ammonium ferric citrate toward high exposure of Fe-N active sites for efficient oxygen and carbon dioxide electroreduction. *Nano Energy* **2017**, *38*, 281–289.
- (22) Sheng, J.; Wang, L.; Deng, L.; Zhang, M.; He, H.; Zeng, K.; Tang, F.; Liu, Y.-N. MOF-Templated Fabrication of Hollow Co₄N@N-Doped Carbon Porous Nanocages with Superior Catalytic Activity. *ACS Appl. Mater. Interfaces* **2018**, *10*, 7191–7200.
- (23) Guo, Z.; Zhang, Z.; Li, Z.; Dou, M.; Wang, F. Well-defined gradient Fe/Zn bimetal organic framework cylinders derived highly efficient iron- and nitrogen- codoped hierarchically porous carbon electrocatalysts towards oxygen reduction. *Nano Energy* **2019**, *57*, 108–117.
- (24) Xia, W.; Zou, R.; An, L.; Xia, D.; Guo, S. A metal-organic framework route to in situ encapsulation of Co@Co₃O₄@C core@shell nanoparticles into a highly ordered porous carbon matrix for oxygen reduction. *Energy Environ. Sci.* **2015**, *8*, 568–576.
- (25) Wu, M.; Wang, K.; Yi, M.; Tong, Y.; Wang, Y.; Song, S. A Facile Activation Strategy for an MOF-Derived Metal-Free Oxygen Reduction Reaction Catalyst: Direct Access to Optimized Pore Structure and Nitrogen Species. *ACS Catal.* **2017**, *7*, 6082–6088.
- (26) Song, Z.; Liu, W.; Cheng, N.; Norouzi Banis, M.; Li, X.; Sun, Q.; Xiao, B.; Liu, Y.; Lushington, A.; Li, R.; Liu, L.; Sun, X. Origin of the high oxygen reduction reaction of nitrogen and sulfur co-doped MOF-derived nanocarbon electrocatalysts. *Mater. Horiz.* **2017**, *4*, 900–907.
- (27) Liu, Y.; Huang, B.; Lin, X.; Xie, Z. Biomass-derived hierarchical porous carbons: boosting the energy density of supercapacitors via an ionothermal approach. *J. Mater. Chem. A* **2017**, *5*, 13009–13018.
- (28) Zhao, H.; Sun, C.; Jin, Z.; Wang, D.-W.; Yan, X.; Chen, Z.; Zhu, G.; Yao, X. Carbon for the oxygen reduction reaction: a defect mechanism. *J. Mater. Chem. A* **2015**, *3*, 11736–11739.
- (29) Jiang, R.; Li, L.; Sheng, T.; Hu, G.; Chen, Y.; Wang, L. Edge-Site Engineering of Atomically Dispersed Fe-N₄ by Selective C-N Bond Cleavage for Enhanced Oxygen Reduction Reaction Activities. *J. Am. Chem. Soc.* **2018**, *140*, 11594–11598.
- (30) Tang, C.; Wang, H.-F.; Chen, X.; Li, B.-Q.; Hou, T.-Z.; Zhang, B.; Zhang, Q.; Titirici, M.-M.; Wei, F. Topological Defects in Metal-Free Nanocarbon for Oxygen Electrocatalysis. *Adv. Mater.* **2016**, *28*, 6845–6851.
- (31) Tang, C.; Wang, H.-F.; Zhang, Q. Multiscale Principles To Boost Reactivity in Gas-Involving Energy Electrocatalysis. *Acc. Chem. Res.* **2018**, *51*, 881–889.
- (32) Cravillon, J.; Nayuk, R.; Springer, S.; Feldhoff, A.; Huber, K.; Wiebcke, M. Controlling Zeolitic Imidazolate Framework Nano- and Microcrystal Formation: Insight into Crystal Growth by Time-Resolved In Situ Static Light Scattering. *Chem. Mater.* **2011**, *23*, 2130–2141.
- (33) Kresse, G.; Hafner, J. Ab initio molecular dynamics for liquid metals. *Phys. Rev. B: Condens. Matter Mater. Phys.* **1993**, *47*, 558–561.
- (34) Kresse, G.; Hafner, J. Ab initio molecular-dynamics simulation of the liquid-metal-amorphous-semiconductor transition in germanium. *Phys. Rev. B: Condens. Matter Mater. Phys.* **1994**, *49*, 14251–14269.

- (35) Kresse, G.; Furthmüller, J. Efficient iterative schemes for ab initio total-energy calculations using a plane-wave basis set. *Phys. Rev. B: Condens. Matter Mater. Phys.* **1996**, *54*, 11169–11186.
- (36) Kresse, G.; Furthmüller, J. Efficiency of ab-initio total energy calculations for metals and semiconductors using a plane-wave basis set. *Comput. Mater. Sci.* **1996**, *6*, 15–50.
- (37) Blöchl, P. E. Projector augmented-wave method. *Phys. Rev. B: Condens. Matter Mater. Phys.* **1994**, *50*, 17953–17979.
- (38) Kresse, G.; Joubert, D. From ultrasoft pseudopotentials to the projector augmented-wave method. *Phys. Rev. B: Condens. Matter Mater. Phys.* **1999**, *59*, 1758–1775.
- (39) Perdew, J. P.; Burke, K.; Ernzerhof, M. Generalized Gradient Approximation Made Simple. *Phys. Rev. Lett.* **1996**, *77*, 3865–3868.
- (40) Monkhorst, H. J.; Pack, J. D. Special points for Brillouin-zone integrations. *Phys. Rev. B: Solid State* **1976**, *13*, 5188–5192.
- (41) Raymundo-Piñero, E.; Azais, P.; Cacciaguerra, T.; Cazorla-Amorós, D.; Linares-Solano, A.; Béguin, F. KOH and NaOH activation mechanisms of multiwalled carbon nanotubes with different structural organisation. *Carbon* **2005**, *43*, 786–795.
- (42) Xia, K.; Wu, Z.; Xuan, C.; Xiao, W.; Wang, J.; Wang, D. Effect of KOH etching on the structure and electrochemical performance of SiOC anodes for lithium-ion batteries. *Electrochim. Acta* **2017**, *245*, 287–295.
- (43) He, Y.; Hwang, S.; Cullen, D. A.; Uddin, M. A.; Langhorst, L.; Li, B.; Karakalos, S.; Kropf, A. J.; Wegener, E. C.; Sokolowski, J.; Chen, M.; Myers, D.; Su, D.; More, K. L.; Wang, G.; Litster, S.; Wu, G. Highly active atomically dispersed CoN₄ fuel cell cathode catalysts derived from surfactant-assisted MOFs: carbon-shell confinement strategy. *Energy Environ. Sci.* **2019**, *12*, 250–260.
- (44) Downes, C. A.; Marinescu, S. C. Electrocatalytic Metal–Organic Frameworks for Energy Applications. *ChemSusChem* **2017**, *10*, 4374–4392.
- (45) Cheng, N.; Banis, M. N.; Liu, J.; Riese, A.; Li, X.; Li, R.; Ye, S.; Knights, S.; Sun, X. Extremely stable platinum nanoparticles encapsulated in a zirconia nanocage by area-selective atomic layer deposition for the oxygen reduction reaction. *Adv. Mater.* **2015**, *27*, 277–281.
- (46) Cheng, N.; Shao, Y.; Liu, J.; Sun, X. Electrocatalysts by atomic layer deposition for fuel cell applications. *Nano Energy* **2016**, *29*, 220–242.
- (47) Gupta, S.; Zhao, S.; Ogoke, O.; Lin, Y.; Xu, H.; Wu, G. Engineering Favorable Morphology and Structure of Fe-N-C Oxygen-Reduction Catalysts through Tuning of Nitrogen/Carbon Precursors. *ChemSusChem* **2017**, *10*, 774–785.
- (48) Huang, B.; Liu, Y.; Xie, Z. Biomass derived 2D carbons via a hydrothermal carbonization method as efficient bifunctional ORR/HER electrocatalysts. *J. Mater. Chem. A* **2017**, *5*, 23481–23488.
- (49) Lv, Y.; Zhang, F.; Dou, Y.; Zhai, Y.; Wang, J.; Liu, H.; Xia, Y.; Tu, B.; Zhao, D. A comprehensive study on KOH activation of ordered mesoporous carbons and their supercapacitor application. *J. Mater. Chem.* **2012**, *22*, 93–99.
- (50) Liang, H.-W.; Zhuang, X.; Brüller, S.; Feng, X.; Müllen, K. Hierarchically porous carbons with optimized nitrogen doping as highly active electrocatalysts for oxygen reduction. *Nat. Commun.* **2014**, *5*, 4973–4980.
- (51) Guo, D.; Shibuya, R.; Akiba, C.; Saji, S.; Kondo, T.; Nakamura, J. Active sites of nitrogen-doped carbon materials for oxygen reduction reaction clarified using model catalysts. *Science* **2016**, *351*, 361–365.
- (52) Geng, D.; Chen, Y.; Chen, Y.; Li, Y.; Li, R.; Sun, X.; Ye, S.; Knights, S. High oxygen-reduction activity and durability of nitrogen-doped graphene. *Energy Environ. Sci.* **2011**, *4*, 760–764.
- (53) Jiao, Y.; Zheng, Y.; Jaroniec, M.; Qiao, S. Z. Origin of the Electrocatalytic Oxygen Reduction Activity of Graphene-Based Catalysts: A Roadmap to Achieve the Best Performance. *J. Am. Chem. Soc.* **2014**, *136*, 4394–4403.
- (54) Liang, J.; Du, X.; Gibson, C.; Du, X. W.; Qiao, S. Z. N-Doped Graphene Natively Grown on Hierarchical Ordered Porous Carbon for Enhanced Oxygen Reduction. *Adv. Mater.* **2013**, *25*, 6226–6231.
- (55) Huang, B.; Liu, Y.; Huang, X.; Xie, Z. Multiple heteroatom-doped few-layer carbons for the electrochemical oxygen reduction reaction. *J. Mater. Chem. A* **2018**, *6*, 22277–22286.
- (56) Liu, Y.; Huang, B.; Zhang, X.; Huang, X.; Xie, Z. In-situ fabrication of nitrogen-doped carbon nanosheets containing highly dispersed single iron atoms for oxygen reduction reaction. *J. Power Sources* **2019**, *412*, 125–133.
- (57) Wang, Q.; Chen, Z.; Wu, N.; Wang, B.; He, W.; Lei, Y.; Wang, Y. N-Doped 3D Carbon Aerogel with Trace Fe as an Efficient Catalyst for the Oxygen Reduction Reaction. *ChemElectroChem* **2017**, *4*, 514–520.
- (58) Zhang, L.; Yang, H.; Wanigarathna, D. K. J. A.; Liu, B. Ultrasmall Transition Metal Carbide Nanoparticles Encapsulated in N, S-Doped Graphene for All-pH Hydrogen Evolution. *Small Methods* **2018**, *2*, 1700353–1700360.
- (59) Li, D.; Jia, Y.; Chang, G.; Chen, J.; Liu, H.; Wang, J.; Hu, Y.; Xia, Y.; Yang, D.; Yao, X. A Defect-Driven Metal-free Electrocatalyst for Oxygen Reduction in Acidic Electrolyte. *Chem* **2018**, *4*, 2345–2356.
- (60) Su, D. S.; Perathoner, S.; Centi, G. Nanocarbons for the development of advanced catalysts. *Chem. Rev.* **2013**, *113*, 5782–5816.
- (61) Cheng, Q.; Han, S.; Mao, K.; Chen, C.; Yang, L.; Zou, Z.; Gu, M.; Hu, Z.; Yang, H. Co nanoparticle embedded in atomically-dispersed Co-N-C nanofibers for oxygen reduction with high activity and remarkable durability. *Nano Energy* **2018**, *52*, 485–493.